DOI: 10.1002/((please add manuscript number))
**Article type: Communication**

# Electrically and Thermally Tunable Smooth Silicon Metasurfaces for Broadband Terahertz Antireflection

*Lu Ding*[*], *Xianshu Luo, Liang Cheng, Maung Thway, Junfeng Song, Soo Jin Chua, Elbert E. M. Chia, Jinghua Teng*[*]

Dr. L. Ding, Dr. J. H. Teng
Institute of Materials Research and Engineering, Agency for Science, Technology and Research (A*STAR), 2 Fusionopolis Way, Innovis, 138634, Singapore
Emails: dingl@imre.a-star.edu.sg; jh-teng@imre.a-star.edu.sg
Dr. X. Luo
Institute of Microelectronics, Agency for Science, Technology and Research (A*STAR), 2 Fusionopolis Way, Innovis, 138634, Singapore
Dr. L. Cheng, Prof. Elbert E. M. Chia
Division of Physics and Applied Physics, School of Physical & Mathematical Sciences, Nanyang Technological University, 637371 Singapore
M. Thway, Prof. S. J. Chua
Department of Electrical and Computer Engineering, National University of Singapore, 11758 Singapore
Prof. J. F. Song
State Key Laboratory on Integrated Opto-Electronics, College of Electronic Science and Engineering, Jilin University, Changchun 130012, People's Republic of China

Keywords: terahertz optics, broadband antireflection, tunable metasurfaces, silicon photonics

Researches in metamaterials and metasurfaces have significant impact on development of terahertz optics and progression of terahertz science and technologies.[1, 2] Further advancement of terahertz systems demands efficient and versatile tunable and reconfigurable metadevices for manipulating various properties of terahertz radiation.[3] Here we demonstrate an electrically and thermally tunable silicon metasurface for broadband terahertz antireflection application. Silicon metasurface is composed by interdigitated p-n junctions fabricated using a completely complementary metal-oxide-semiconductor (CMOS) compatible process in a silicon photonics foundry. It is atomically smooth without any physically etched pattern nor metal antennas. By supplying bias voltage to p-n junctions, complex reflection coefficient of silicon metasurface is continuously tuned between negative and positive values. Complete antireflection condition can be precisely achieved, represented

by the vanishing of the echo pulse in terahertz time-domain spectroscopy. Transmission amplitude is bias-polarity dependent, while the phase is simultaneously manipulated. The active silicon metasurface has a unique property that it thermally tunes the reflection and electrically tunes transmission. The methodology suggests a new design concept using all-silicon platform for making atomically smooth and electrically controlled metadevices in terahertz and other frequency range.

Metasurfaces are constructed by a thin layer of subwavelength in-plane functional building blocks for manipulating amplitude and phase of the electromagnetic radiation.[2] Active metasurfaces, which are controlled by electrical bias voltage,[4-6] temperature,[7] magnetic field,[8] optical pumping,[9, 10, 11] or mechanical deformation,[12] etc., further extend their designed passive properties by allowing new functionalities or fine tuning to the operational conditions. Recently, various active terahertz metadevices have been demonstrated, such as filters,[9] switches,[6, 11] and modulators via phase,[5] amplitude,[4] and frequency modulation.[10] Versatile functionalities are realized by integrating metasurfaces with functional materials, e.g., graphene,[6] semiconductor two-dimensional electron gas system,[4] and semiconductor hybridized in metamaterial scatterers,[5, 13] etc. Owing to the quasi-planar nature, metasurfaces and metadevices are readily fabricated using planar micro-/nano-patterning techniques, such as lithography, focused ion-beam, and nanoimprinting. Amongst various demonstrations, silicon-based active metadevices are rarely reported despite the facts that silicon is one of the most popular materials used for fabricating terahertz optics and is recently becoming a promising material for metasurfaces applications.[14] Furthermore, fabrication of silicon-based photonic devices is completely CMOS compatible with manufacturability, thus low cost, scalability, and integration potential with various functional photonic architectures.

As one important application, metasurface has been applied to design broadband THz antireflection coating,[15] which is to remove undesired reflection in THz optical systems. Various broadband THz antireflection techniques have been developed in the past,[16] mainly using gradient index matching, metamaterials and metasurfaces, as well as impedance matching. Traditional gradient index matching shows both the transmission enhancement and reflection reduction. However, it either strictly impose requirements on the film thickness and refractive index matching, or utilize complicated fabrication processes and create non-planar surface structures which hinder the device integration. Novel metamaterials and metasurfaces results in enhanced transmission and reduced reflection within limited bandwidth. Using simple impedance matching method, the Fabry-Perot fringes can be completely suppressed over a broadband range, up to 10 THz. The major tradeoff is the power loss in transmission due to resistive losses (positive conductance). Therefore, to combine both broadband and tunable functionalities, one of the solutions is to combine metasurface and impedance matching. In addition, it is challenging to have an as-fabricated coating to precisely fulfill the precise antireflection condition. It can be addressed using an antireflection coating with actively controlled reflection coefficient, which has yet been demonstrated. In this paper, we present a novel atomically smooth silicon metasurface for tunable broadband antireflection application. The design consists of interdigitated p-n junctions, which continuously tunes the complex reflection coefficient of silicon metasurface by supplying bias voltage. Antireflection condition is precisely achieved via impedance matching. The fabrication is CMOS-compatible and scalable using existing silicon photonics fabrication platform. Furthermore, electrical control of the silicon metadevices is simple and direct which is much favored in the market.

Schematic of the active silicon antireflection coating is shown in **Figure 1**a. The substrate is double side polished high resistivity float zone silicon (HRFZ Si) which is highly transparent in a broadband terahertz range.[17] Silicon metasurface consists of interdigitated p-

n junctions, namely, alternating p- and n-type silicon stripes with one dimensional deep-subwavelength periodicity covering the entire surface using ion implantation. One period is composed of one p-doped and one n-doped stripes with identical width (**Figure 1**b). The p- and n-type doping has peak concentration of $4\times10^{19}$ $cm^{-3}$ and $7\times10^{19}$ $cm^{-3}$ respectively, and implantation depth of ~ 500 nm (Supporting Information, **Figure S**1). All p- and n-doped stripes are separately connected to the corresponding perpendicular p++ and n++ Ohmic contacts for bias voltage control.

The interdigitated doping pattern is investigated by mid-infrared nano-imaging at 990 $cm^{-1}$ via a scattering-type scanning near-field optical microscope (s-SNOM) (Supporting Information, **Figure S**2).[18] Atomic force microscope (AFM) topography *z* (**Figure 1**c) and line plot (**Figure 1**d) show no obvious periodicity correlated with the doping pattern. Surface roughness is $R_a$ ~ 0.24 nm, extracted from **Figure 1**d. Therefore, ion implantation introduces very little surface crystalline damage, suggesting an atomically smooth surface. On the contrary, optical amplitude $s_4$ and phase $\varphi_4$, which are simultaneously attained with *z*, show periodic optical contrast which is identical to the design of the silicon metasurface (**Figures 1**e,g). The contrast comes from the difference in complex dielectric function of doped silicon with different doping concentration.[18] Depletion region between p-n junctions is clearly resolved in line plots of $s_4$ and $\varphi_4$ (**Figures 1**f,h), which has width about 500 ± 50 nm. Phase transition between adjacent doped regions is slightly asymmetric, reflecting a lateral relative shift of 100 nm between p- and n-type regions. It is attributed to misalignment during two successive ion-implantation process, which corresponds to the alignment accuracy of ± 120 nm.

Transmission THz time-domain spectroscopy (THz-TDS) is applied to characterize the device with respect to bias voltage and bias polarity. The schematics of the setup is shown in **Figure 2**a. THz-TDS is carried out using a commercial terahertz system (Menlo TERA K15).

THz beam is vertically polarized with the spectral range from 0.1 to 3 THz. THz beam is focused on sample via TPX50 lens with 50 mm effective focal length. The system is in an enclosure purged with $N_2$ gas to avoid the absorption from atmospheric water vapor. The device is mounted in TE configuration, where the longer side of silicon stripe parallel with the polarization of the incident THz wave, because that the metasurface has one dimensional periodicity. The device is centered and glued on an aluminum holder with a hole (diameter is 4 mm). The electrodes of the device are wire bonded to a customized PCB board for supplying bias voltage though a DC power supply (HP 6633A 0 – 50 V / 0 – 2 A). The transmitted time signal is integrated 20 s to improve the signal-to-noise ratio.

Time domain traces of the first two THz pulses are recorded under various bias voltages, where $P_1$ is the main pulse (**Figure** 2b) and $P_2$ is the first echo pulse (**Figure** 2c). Entire time domain traces are given in Supporting Information, **Figure S**3a. Precise antireflection condition is characterized by the vanishing of $P_2$. The amplitude spectra are calculated by the Fast Fourier Transform (FFT) of the temporal waveform of the detected THz pulses (**Figure** 2d). At 0 V, $P_1$ and $P_2$ have phase inverted with each other indicating that the impedance of air has been over compensated by the unbiased silicon metasurface [19]. The amplitude spectrum shows clear Fabry-Perot interference fringes. With increasing reverse (-) bias, $P_1$ has its amplitude increased and phase delayed, while $P_2$ has amplitude decreased to about zero at -25 V bias then increased at -40 V bias with phase inversion. The amplitude spectra increases when interference fringes are firstly reduced then increased to an opposite phase (**Figure** 2d). The response of device under forward (+) bias is similar to that under reverse bias, except that the amplitude of $P_1$ decreases. In summary, $P_2$ is tuned by bias voltage within a range including the precise antireflection condition, regardless of bias polarity. Whereas, amplitude of $P_1$ is bias-polarity dependent and phase of $P_1$ is simultaneously tuned by bias voltage over a broadband THz range.

The device clearly shows the voltage-dependent antireflection and both amplitude and phase of terahertz pulses are continuously tuned. To further understand origins of the tunability, complex reflection coefficient $\tilde{r_c}$ of silicon metasurface is summarized as a function of bias voltage (**Figure 3**a,b), where amplitude $|r_C|$ and phase $\varphi_C$ are given by $\tilde{r_c} = |r_c|e^{i\varphi_C} = e^{-i2kL}\, 1/r_{Si}\, (P_2/P_1)$, where $e^{-i2kL}$ is the round trip phase shift in the silicon substrate. In TE configuration, $|r_C|$ continuously decreases to zero then increases and $\varphi_C$ continuously changes from $\pi$ to 0 while absolute voltage increases. At zero bias, $\varphi_C$ is $\pi$. Precise antireflection condition ($\varphi_C = \pi/2$, red line in **Figure 3**b) is achievable regardless the bias polarity. Therefore, tuning in $\tilde{r_c}$ is attributed to thermo-optical effect due to Joule heating (Supporting Information, **S**3-5). When biasing the silicon metasurface, 100% of electric power is converted to dissipated power due to the large series resistance in p- and n-regions (Supporting Information, **S**6). **Figure 3**a superimposes surface temperature of the device at corresponding voltage. Sheet conductivity of pure p- and n-doped silicon decreases with increasing temperature, the impedance mismatching between silicon and air is reduced and so complete antireflection is achieved (Supporting Information, **S**7). In TM configuration, both $|r_C|$ and $\varphi_C$ have less dependence on bias voltage (time domain traces in TM configuration is provided in Supporting Information, **S**8). It is understood that the depletion region blocks the carriers' movement to adjacent doped regions so that terahertz wave is less influenced by the carriers.

**Figure 3**c plots a relative time shift of $P_1$ ($\Delta t_{P_1} = t_{P_1}^{Bias} - t_{P_1}^{0V}$) with respect to dissipated power. In general, $P_1$ is linearly dependent on power dissipation and independent on polarization and bias polarity. An error bar of ±10 fs is included by repeating measurements. Taken slope $\partial t/\partial P$=7.5 fs/W and average Joule heating rate $\partial T/\partial P$=15 K/W (Supporting Information, S6), thermo-optic coefficient $\frac{1}{n}\frac{\partial n}{\partial T}$ of silicon is then calculated as $6.1\times10^{-5}$ $K^{-1}$

from relation $\frac{\partial t}{\partial P} = \frac{L}{c}\frac{\partial n}{\partial T}\frac{\partial T}{\partial P}$. It agrees fairly well with reported values.[20] Therefore, $\Delta t_{P_1}$ is attributed to thermally induced refractive index change in the silicon substrate.

**Figure 3**d shows the normalized amplitude variation of $P_1$ ($\Delta A_{P_1}/A_{P_1}^{0V} = \left(A_{P_1}^{Bias} - A_{P_1}^{0V}\right)/A_{P_1}^{0V}$) as a function of bias voltage. $\Delta A_{P_1}/A_{P_1}^{0V}$ is bias polarity dependent with a negative sign of voltage. Total variation of transmission amplitude in TE configuration is ~ 13% between -40 V and +20 V. Further increasing voltage results in fast decreasing of $\Delta A_{P_1}/A_{P_1}^{0V}$ which is attributed to the breakdown of p-n junctions in reverse bias and unstable IV performance due to overheating in forward bias. Theoretically, the upper limit of transmission for impedance-matched antireflection coating is affected by the imaginary part of the conductivity.[21] Since the carrier type and concentration is different under reverse and forward bias, it modifies the effective terahertz conductivity of the silicon metasurface, especially the imaginary part. Therefore, the active silicon metasurface has a unique property that it thermally tunes the reflection and electrically tunes transmission.

In conclusion, we demonstrate an electrical bias voltage controlled silicon metasurface for broadband terahertz antireflection application, where the reflection coefficient can be continuously tuned and transmission has unique bias-polarity dependence. Complete antireflection condition can be precisely achieved. The tuning range in transmission can be further expanded by improving design of the junction region as well as magnifying the electrical tuning and reducing the thermal tuning. Further exploitation on independently biasing the p-n junctions or designing modular functions may lead to programmable metamaterials proposed recently.[22] The CMOS compatibility and smooth nature of the metasurface facilitate its potentially monolithic integration with other planar optical components for applications in terahertz and other frequency regime. It also links active metasurface research with existing silicon integrated photonic architectures,[23] which would bring new possibility to realize novel and complex optical systems using metasurfaces.

**Experimental Section**

*Device fabrication:* The interdigitated p-n junction diodes are fabricated on an 8 inches silicon wafer through standard CMOS process in IME's (Institute of Microelectronics, Agency for Science, Technology and Research (A*STAR)) silicon photonics line.[24] The wafer is double side polishing and has a thickness of 725 ± 15 μm. It is slightly p-doped with Boron with bulk resistivity of $\rho_{substrate}$ = 5 KΩ·cm. The p-n junction is formed by using standard implantation with Boron and Phosphorus as the dopants respectively. Period Λ is 5 μm and width W is 2.5 μm (**Figure 1**b). Doping concentrations of p++ and n++ Ohmic contacts are higher than $1\times10^{20}$ $cm^{-3}$. Rapid thermal annealing is applied to activate the dopants. A 500 nm cladding oxide is deposited by plasma-enhanced chemical vapor deposition, followed with contact hole opening to p++ and n++ regions. Aluminum with 750 nm in thickness is deposited and patterned to form the contact pads. The cladding oxide is completely etched in the interdigitated p-n area to form a THz transmission window of 5×5 $mm^2$. Finally, the wafer is mechanically diced and individual device is wire-bonded for electrically testing.

*Mid-infrared near-field imaging:* Near field images are obtained by a commercial s-SNOM (Neaspec GmbH) (Supporting Information, **Figure S**2). Mid-infrared laser source is a quantum cascade laser operating at 990 $cm^{-1}$. Scanning area is 10×5 μm by 600×100 pixels. The experiment is performed at ambient conditions.

*Temperature dependent THz-TDS spectroscopy:* The measurement uses a commercial terahertz system (TPS Spectra 3000) (Supporting Information, **Figure S**6), providing a bandwidth from 0.1 to 3 THz. The acquired data were averaged from 900 spectra with a scanning frequency of 30 Hz, which gave a very high signal to noise ratio. Spectral resolution is 0.2 $cm^{-1}$. Temperature range is from 300 to 350 K.

*Voltage-temperature measurement:* Surface temperature of the biased sample is measured by a contact thermometer (TKDT 10), while sample is mounted in the same way as in bias-voltage-dependent THz-TDS measurement.

**Supporting Information**,
Supporting Information, is available from the Wiley Online Library or from the author.

**Acknowledgement**

The authors thank J.N.Wang for valuable discussions on the device transport physics, D.V.M.Repaka, H.K.Ng, K.Hippalgaonkar, H.W.Liu, N.Zhang and L.Ke for sharing tools for the device characterization, A.Cernescu for discussions and technical support on the use of MIR s-SNOM, and C.M.Ke for discussion on device simulation. The work was financially supported by the Institute of Materials Research and Engineering and the Agency for Science, Technology and Research (A*STAR) under Grant No. 152 7000014.

Received: ((will be filled in by the editorial staff))
Revised: ((will be filled in by the editorial staff))
Published online: ((will be filled in by the editorial staff))

**References**

[1] a) M. Tonouchi, *Nat. Photon.* **2007**, 1, 97; b) X. C. Zhang, A. Shkurinov, Y. Zhang, *Nat. Photon.* **2017**, 11, 16.
[2] a) C. L. Holloway, E. F. Kuester, J. A. Gordon, J. O'Hara, J. Booth, D. R. Smith, *IEEE Antennas Propag. Mag.* **2012**, 54, 10; b) H.-T. Chen, A. J. Taylor, N. Yu, *Rep. Prog. Phys.* **2016**, 79, 076401.
[3] M. Rahm, J.-S. Li, W. J. Padilla, *J. Infrared Millim. Terahertz Waves.* **2013**, 34, 1.
[4] T. Kleine-Ostmann, P. Dawson, K. Pierz, G. Hein, M. Koch, *Appl. Phys. Lett.* **2004**, 84, 3555.
[5] H.-T. Chen, W. J. Padilla, M. J. Cich, A. K. Azad, R. D. Averitt, A. J. Taylor, *Nat. Photon.* **2009**, 3, 148.
[6] S. H. Lee, M. Choi, T.-T. Kim, S. Lee, M. Liu, X. Yin, H. K. Choi, S. S. Lee, C.-G. Choi, S.-Y. Choi, *Nat. Mater.* **2012**, 11, 936.
[7] J. Han, A. Lakhtakia, *J. Mod. Opt.* **2009**, 56, 554.
[8] L. Kang, Q. Zhao, H. Zhao, J. Zhou, *Opt. Express* **2008**, 16, 17269.
[9] I. H. Libon, S. Baumgärtner, M. Hempel, N. Hecker, J. Feldmann, M. Koch, P. Dawson, *Appl. Phys. Lett.* **2000**, 76, 2821.
[10] a) H.-T. Chen, J. F. O'Hara, A. K. Azad, A. J. Taylor, R. D. Averitt, D. B. Shrekenhamer, W. J. Padilla, *Nat. Photon.* **2008**, 2, 295; b) L. Deng, J. Teng, H. Liu, Q. Y. Wu, J. Tang, X. Zhang, S. A. Maier, K. P. Lim, C. Y. Ngo, S. F. Yoon, *Adv. Opt. Mater.* **2013**, 1, 128.
[11] D. R. Chowdhury, R. Singh, J. F. O'Hara, H.-T. Chen, A. J. Taylor, A. K. Azad, *Adv. Opt. Mater.* **2011**, 99, 231101.
[12] a) H. Tao, A. C. Strikwerda, K. Fan, W. J. Padilla, X. Zhang, R. D. Averitt, *Phys. Rev. Lett.* **2009**, 103, 147401; b) S. M. Kamali, E. Arbabi, A. Arbabi, Y. Horie, A. Faraon, *Laser Photon. Rev.* **2016**, 10, 1002; c) B. Gupta, S. Pandey, A. Nahata, T. Zhang, A. Nahata, *Adv. Opt. Mater.* **2017**, 5.

[13] H.-T. Chen, W. J. Padilla, J. M. Zide, A. C. Gossard, A. J. Taylor, R. D. Averitt, *Nature* **2006**, 444, 597.
[14] a) I. Staude, J. Schilling, *Nat. Photon.* **2017**, 11, 274; b) M. R. Hashemi, S. Cakmakyapan, M. Jarrahi, *Rep. Prog. Phys.* **2017**.
[15] a) H.-T. Chen, J. Zhou, J. F. O'Hara, F. Chen, A. K. Azad, A. J. Taylor, *Phys. Rev. Lett.* **2010**, 105, 073901; b) L. Ding, Q. Y. S. Wu, J. H. Teng, *Laser Photon. Rev.* **2014**, 8, 941; c) H.-T. Chen, C.-C. Chang, L. Huang, presented at 42nd IRMMW-THz, Mexico, Aug. **2017**.
[16] a) Y.-F. Huang, S. Chattopadhyay, Y.-J. Jen, C.-Y. Peng, T.-A. Liu, Y.-K. Hsu, C.-L. Pan, H.-C. Lo, C.-H. Hsu, Y.-H. Chang, C.-S. Lee, K.-H. Chen, L.-C. Chen, *Nat. Nanotechnol.* **2007**, 2, 770; b) L. Ding, X. Wang, N. S. S. Ang, C. Lu, V. Suresh, S.-J. Chua, J. Teng, *IEEE J. Sel. Topics Quantum Electron.* **2017**, 23, 1.
[17] J. Dai, J. Zhang, W. Zhang, D. Grischkowsky, *J. Opt. Soc. Am. B* **2004**, 21, 1379.
[18] A. J. Huber, D. Kazantsev, F. Keilmann, J. Wittborn, R. Hillenbrand, *Adv. Mater.* **2007**, 19, 2209.
[19] A. Thoman, A. Kern, H. Helm, M. Walther, *Phys. Rev. B* **2008**, 77, 195405.
[20] H. Li, *J. Phys. Chem. Ref. Data* **1980**, 9, 561.
[21] G. Jnawali, Y. Rao, H. Yan, T. F. Heinz, *Nano Lett.* **2013**, 13, 524.
[22] a) T. J. Cui, M. Q. Qi, X. Wan, J. Zhao, Q. Cheng, *Light Sci. Appl.* **2014**, 3, e218; b) S. Liu, T. J. Cui, Q. Xu, D. Bao, L. Du, X. Wan, W. X. Tang, C. Ouyang, X. Y. Zhou, H. Yuan, *Light Sci. Appl.* **2016**, 5, e16076; c) S. Liu, T. J. Cui, L. Zhang, Q. Xu, Q. Wang, X. Wan, J. Q. Gu, W. X. Tang, M. Qing Qi, J. G. Han, *Adv. Sci.* **2016**, 3, 1600156; d) S. Liu, T. J. Cui, *Adv. Opt. Mater.* **2017**, 5, 1700624.
[23] A. W. Poon, X. Luo, F. Xu, H. Chen, *Proc. IEEE* **2009**, 97, 1216.
[24] A. E.-J. Lim, J. Song, Q. Fang, C. Li, X. Tu, N. Duan, K. K. Chen, R. P.-C. Tern, T.-Y. Liow, *IEEE J. Sel. Topics Quantum Electron.* **2014**, 20, 405.

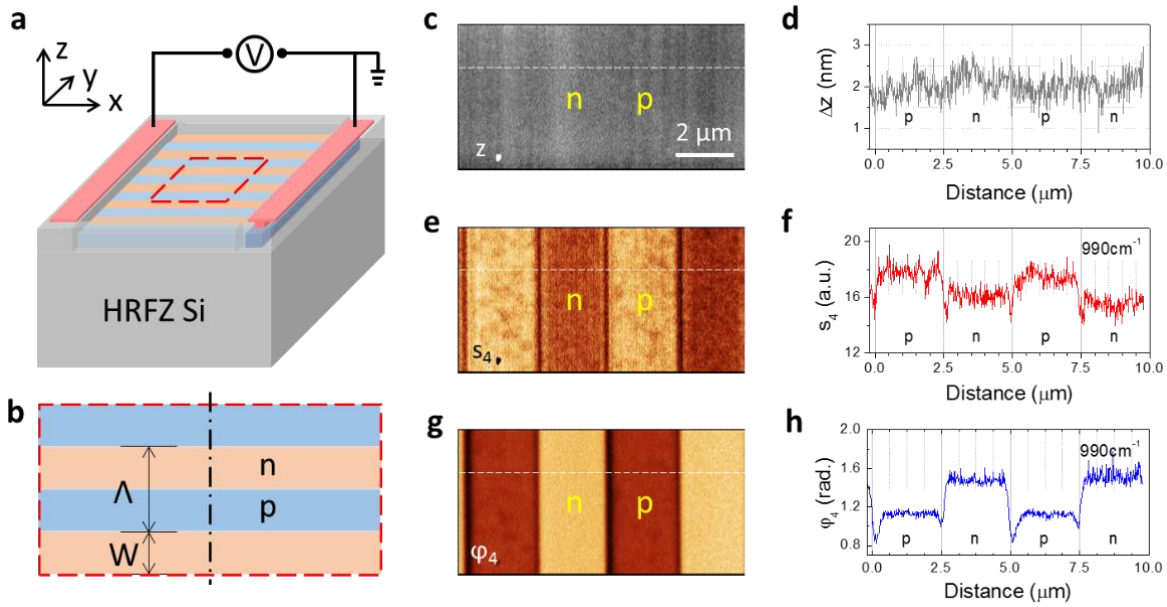


**Figure 1.** a) Schematic of the device. b) Zoom-in top view of the silicon metasurface. Λ is the period and W is the width of the p-/n-type silicon stripe. c-h) Real-space mid-infrared s-SNOM imaging of the silicon metasurface taken in a single scan at wavenumber 990 $cm^{-1}$. AFM topographic image (c) and a line plot (d) extracted from the dashed line in (c). Optical amplitude signal $s_4$ of the interdigitated p-n junctions (e) and a line plot (f) extracted from the dashed line in (e). Optical phase signal $\varphi_4$ of the interdigitated p-n junctions (g) and a line plot (h) extracted from the dashed line in (g). The p- and n-type regions are identified by correlating the scanning images with the mask design.

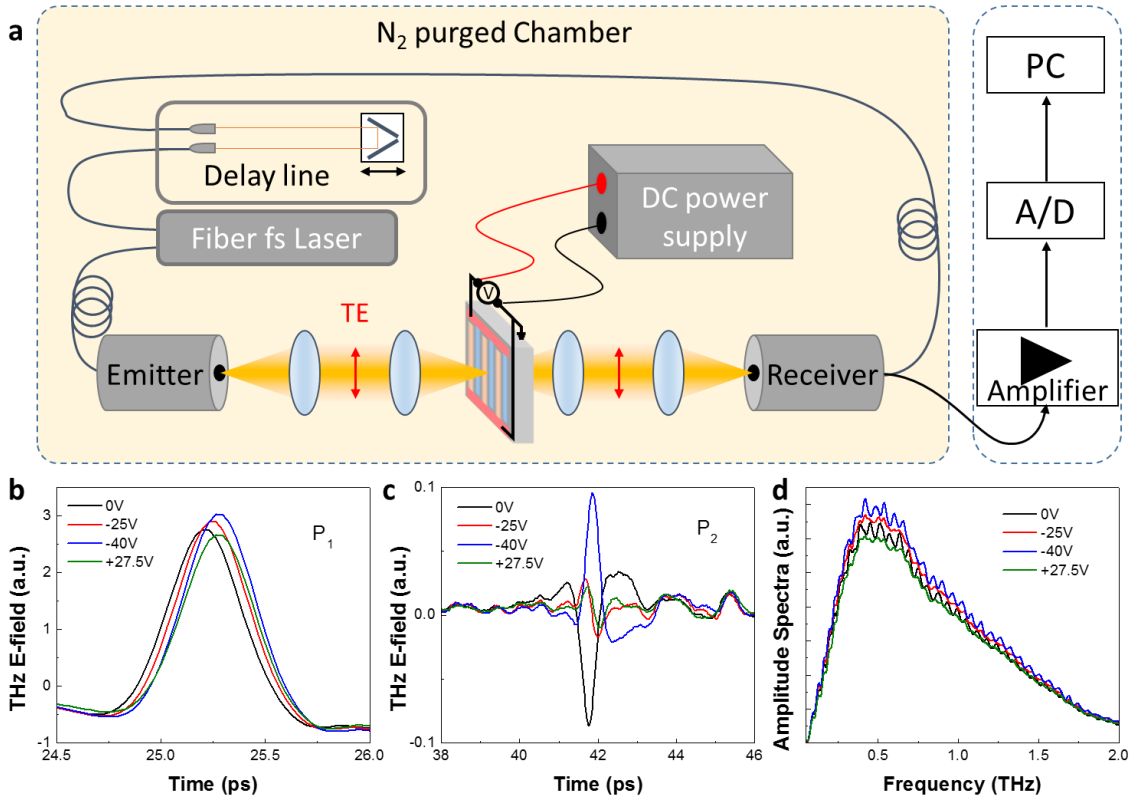


**Figure 2.** a) Schematics of bias-voltage-dependent transmission THz-TDS in TE configuration using Menlo TERA K15. b-d) Time-domain traces of main pulse $P_1$ (b) and the first echo $P_2$ of the silicon substrate (c) at selected bias voltages, and amplitude spectra calculated by FFT (d).

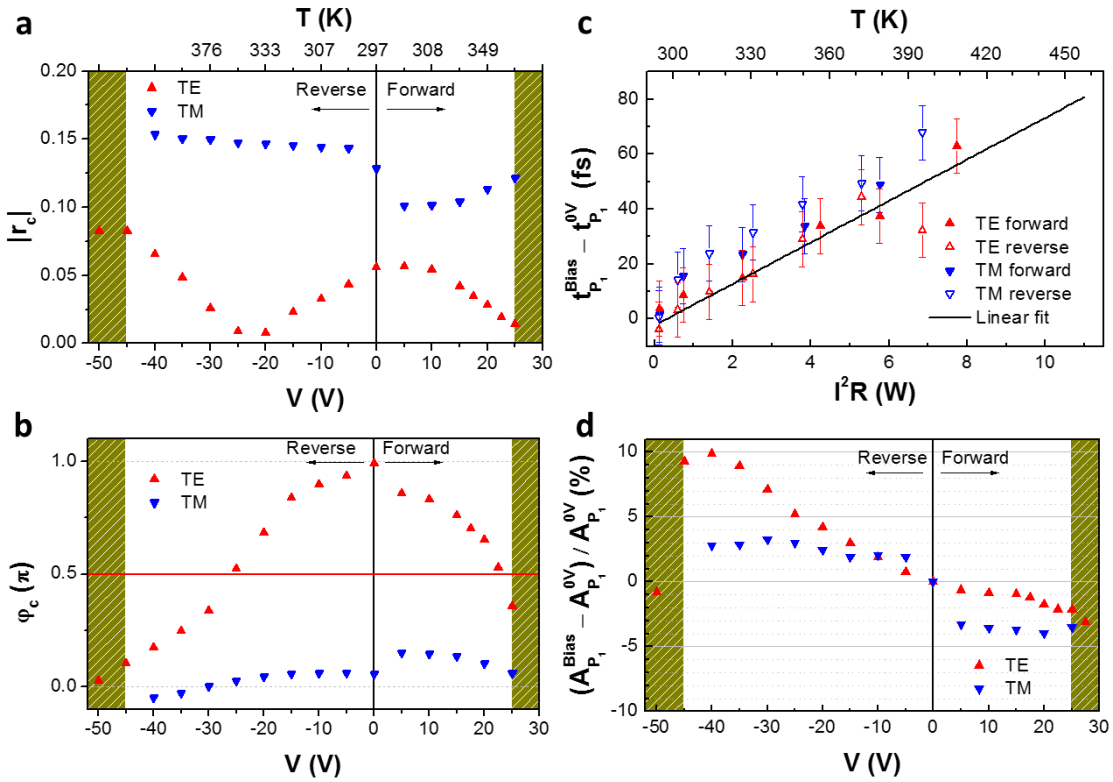


**Figure 3.** a,b) Bias voltage and surface temperature dependent complex reflection coefficient of silicon metasurface at 1.1 THz in TE and TM configurations, amplitude $|r_C|$ (a) and phase $\varphi_C$ (b). c) Relative time delay of $P_1$ as a function of dissipated power ($I^2R$) under forward and reverse bias with respect to that of zero bias in TE and TM configurations. A linear fit with slope $\partial t/\partial P$ = 7.5 fs/W is superimposed. The corresponding surface temperature is indicated in the upper X axis. d) Normalized amplitude variation of $P_1$ with respect to that of zero bias in TE and TM configurations.

((Supporting Information can be included here using this template))

Copyright WILEY-VCH Verlag GmbH & Co. KGaA, 69469 Weinheim, Germany, 2016.

# Supporting Information

## Electrically and Thermally Tunable Smooth Silicon Metasurfaces for Broadband Terahertz Antireflection

*Lu Ding*[*], *Xianshu Luo, Liang Cheng, Maung Thway, Junfeng Song, Soo Jin Chua, Elbert E. M. Chia, Jinghua Teng*[*]

### S1. Ion implantation profile

A thin layer of silicon is doped with Boron or Phosphorus, for p- or n-type doping respectively, by ion implantation. Depth profile of the doping concentration of the selected sample is measured by dynamic secondary ion mass spectrometry (D-SIMS) (**Fig. S1**). Boron has a concentration ~$4\times10^{19}$ $cm^{-3}$ uniformly distributed in the first 100 nm and exponentially decreases to $1\times10^{16}$ $cm^{-3}$ until depth of 550 nm. Phosphorus has a higher concentration of ~$7\times10^{19}$ $cm^{-3}$ uniformly distributed in the first 50 nm depth and faster exponentially decreases to $2\times10^{16}$ $cm^{-3}$ until depth of 450 nm. Analytical error is estimated about 5%~10%. Implantation depth is much smaller than the wavelength of terahertz wave. For antireflection based on impedance matching, the surface of silicon substrate shall have a thin conductive layer with critical sheet conductivity of $d\sigma_{dc}$ = 6.42 mS.[1] Here, the doping concentration is purposely chosen to give rise to a higher effective sheet conductivity than the critical value, so that the impedance of air is over compensated for later active tuning purpose.

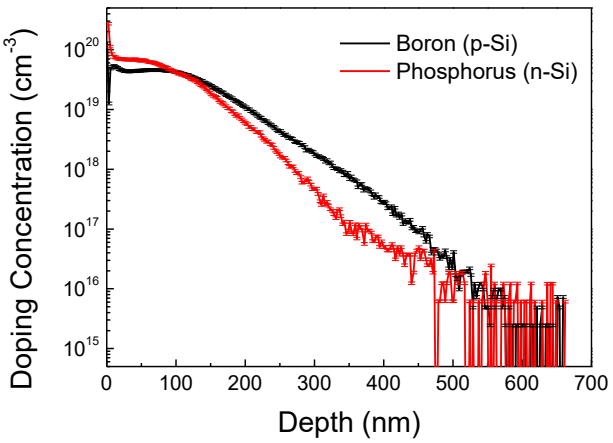


**Fig. S1**. Depth profile of p- and n-Si doping measured by D-SIMS.

### S2. Mid-infrared near-field imaging

The detection scheme of mid-infrared near-field imaging by s-SNOM is shown in **Fig. S2**. It is based on an AFM operating in tapping mode at frequency of $\Omega \approx 250$ kHz and a tapping amplitude of 70 nm. The spatial resolution is about 25 nm defined by the radius of curvature of the AFM tip apex. Mid-infrared laser source is a quantum cascade laser operating at 990 $cm^{-1}$.

A pseudo-heterodyne interferometric detection module is implemented in the s-SNOM to extract both the scattering amplitude (s) and phase (φ) of the near-field signal. To subtract the background signal, we demodulated the near-field signal at the fourth harmonics 4Ω of the tapping frequency. Here, both $s_4$ and $\varphi_4$ signals are as-measured since they are sufficient to describing all the doping characteristics of the silicon metasurface.

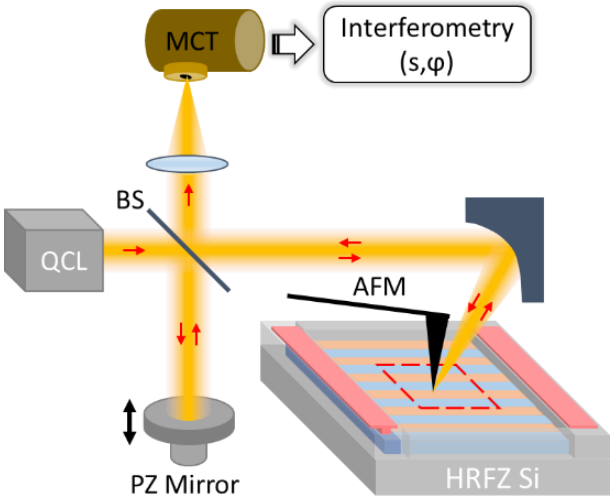


**Fig. S2**. Schematics of mid-infrared near-field imaging using s-SNOM.

## S3. Room temperature passive THz measurement

**Fig. S3**a shows complete time domain traces of silicon, silicon with p-Si thin layer, silicon with n-Si thin layer, and silicon metasurface in TE and TM configurations. Pulse profile of free space terahertz pulse is maintained in silicon, p-Si, n-Si, and silicon metasurface in TE configuration. **Fig. S3**b plots the transmission spectra of $P_1$ normalized to that of silicon calculated by FFT. The broadband nature of p-Si, n-Si, and silicon metasurface in TE configuration is shown since the normalized transmission are flat over the entire spectral range. **Fig. S3**c shows the amplitude $|r_C|$ of the complex reflection coefficient. Up on the general broadband feature of $|r_c|$, there are oscillations more and more significant when $|r_c|$ gets close to zero or to frequency extremes of the THz-TDS system. Such oscillations are also observed in transmission spectra (**Fig. S3**b) at frequency extremes of the THz-TDS system. We attribute the oscillations in reflection and transmission spectra to the bad signal-to-noise ratio when very close to the frequency extremes of the THz-TDS system as well as the weak signal of $P_2$ near complete antireflection condition.

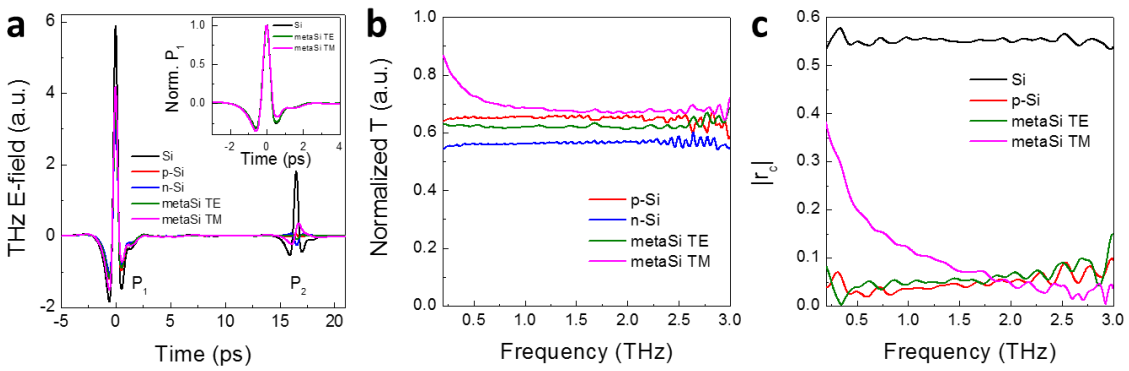


**Fig. S3**. a) Time domain traces of silicon, silicon with p-Si thin layer, silicon with n-Si thin layer, and silicon metasurface in TE and TM configurations. Inset is the comparison of

normalized $P_1$ for silicon and silicon metasurface in TE and TM configurations. b) Transmission spectra of $P_1$ normalized to that of silicon calculated by FFT. c) $|r_C|$ in frequency domain of silicon, silicon with p-Si thin layer, and silicon metasurface in TE and TM configurations.

Silicon (black curve) has strong $P_2$ due to its high refractive index. The reflection coefficient calculated by $r = \sqrt{P_2/P_1} = 0.55$ agrees well with that calculated by the Fresnel equation $\frac{n_{Si}-n_{air}}{n_{Si}+n_{air}} = 0.547$, taking $n_{Si} = 3.4175$ and $n_{air} = 1.0003$.[2]

For p-Si (red curve), $P_1$ is reduced to 65% attributed to free carrier absorption, while $P_2$ is almost vanished due to nearly impedance matching. For n-Si (blue curve), $P_1$ is reduced further to 56% and $P_2$ has inverted phase due to impedance over compensation. Interestingly, it is the doping concentration determines the terahertz response rather than the type of dopant, considering the very similar response of p-Si and n-Si (therefore only $|r_c|$ for p-Si is shown in **Fig. S3**c).

For silicon metasurface, in TE configuration (green curve), $P_1$ is reduced to 62.3% and $P_2$ is inverted. In TM configuration (magenta curve), not only the amplitude of $P_1$ is reduced but also the pulse profile is modified (**Fig. S3**a inset). Transmission monotonically decreases to 68% with increasing frequency and remains at a constant at high frequency (**Fig. S3**b). It is because that the depletion region between p-n junctions acts as an effective gap to stop the free movement of the carriers from adjacent doped regions in TM configuration, which is similar to the case of metal grating.[3] However, the p- and n-type regions are physically close where the depletion region is only a few hundreds of nanometers (**Fig. 1**h). Such periodicity modifies the transmitted pulse profile and the frequency response in TM configuration. The thermal diffusion of implanted ions may slightly blur the boundary and make the situation more unpredictable. This can be qualitatively verified by the FDTD simulation in which the electronic property of individual doped silicon is extracted from **Fig. S3**a.

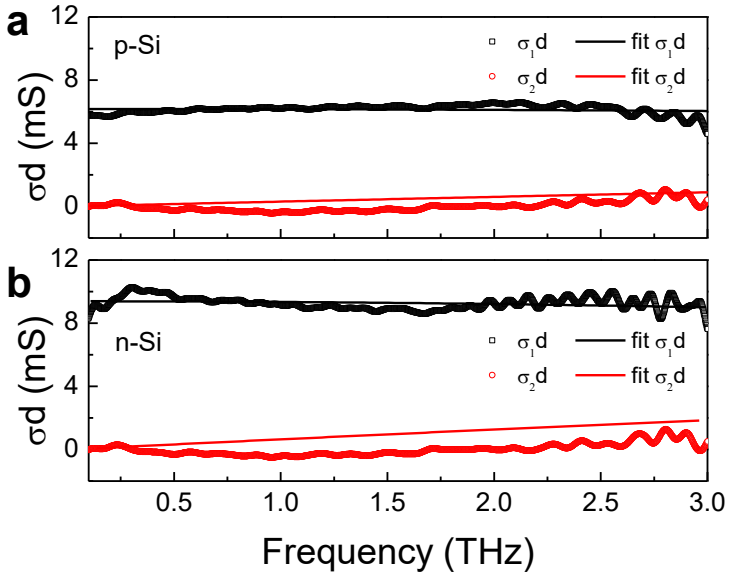


**Fig. S4**. a) Complex sheet conductivity of p-Si thin layer, b) Complex sheet conductivity of n-Si thin layer. Both real and imaginary part of sheet conductivity are fit by Drude model.

The complex sheet conductivity $d\tilde{\sigma}(\omega) = d\sigma_1 + id\sigma_2$ of p-/n-Si thin layer is calculated by comparing the time-dependent electric field of terahertz pulse transmitted through the thin film sample as well as through the uncoated substrate as reference.[4]

$$\frac{E_{Si+film}(\omega)}{E_{Si}(\omega)} = \frac{n_{air} + n_{Si}}{n_{air} + n_{Si} + Z_0 d\tilde{\sigma}(\omega)}, \quad \text{(S1)}$$

where $Z_0 = \sqrt{\mu_0/\varepsilon_0} = 377\Omega$ is the impedance of free space. Due to the complexity of the doping profile, only the sheet conductivity is meaningful. Results are plot in **Figs. S4**a,b. $d\sigma_{dc}$ is extrapolated to be 6.35 and 9.42 mS for p- and n-Si samples respectively. P-Si thin layer is very close to the impedance matching condition ($d\sigma_{dc}$ = 6.42 mS), while n-Si thin layer is over compensated. $d\sigma_{dc}$ of p- and n-Si thin layer is also measured by Van der Pauw (VdP) method to be 6.64 ± 0.02 and 9.68 ± 0.02 mS, respectively. The wafer level uniformity for p- and n-Si is 6.8 ± 0.3 and 9.9 ± 0.3 mS, respectively. Results from both experiments agree well with each other.

The complex conductivity of doped silicon calculated by Eq. (S1) is fit by Drude model[5]

$$\tilde{\sigma}(\omega) = \frac{\varepsilon_0 \omega_p^2 \tau}{1 - i\omega\tau}, \quad \text{(S2)}$$

where the plasma frequency $\omega_p$ is given by $\omega_p^2 = Ne^2/\varepsilon_0 m^*$; N is the carrier density, $m^*$=0.26$m_0$ for the effective electron mass and 0.37$m_0$ for the effective hole mass;[6] $m_0$ is the free electron mass. The relaxation time $\tau$ is given by $\mu = |e|\tau/m^*$; $\mu$ is the electron or hole mobility which is the key fitting parameter. Carrier density is taken from DSIMS results (**Fig. S**1). The fitting electron mobility is 73.9 $cm^2V^{-1}S^{-1}$ and hole mobility is 53.3 $cm^2V^{-1}S^{-1}$, which agrees nicely with literature.[7] Fitting curves show fairly good agreement with experiment. Discrepancy on the imaginary part at high frequency is attributed to the simple model which neglecting the complexity on non-uniform depth profile of doping. Validity of Drude model confirms that doped silicon is metalized for current doping condition. The electronic property of doped silicon thin layer is summarized in **Table S1**.

**Table S1**. Electronic property of doped silicon thin layer

| **Element** | **Type of Dopant** | **Doping Concentration (D-SIMS)** x $10^{14}$ $cm^{-2}$ | $d\sigma_1$ **(VdP)** mS | $d\sigma_1$ **(TDS)** mS | **Mobility (fitting)** $cm^2V^{-1}s^{-1}$ |
|---|---|---|---|---|---|
| **Boron** | p | 7.23 | 6.64±0.02 | 6.35 | 53.3 |
| **Phosphorus** | n | 7.93 | 9.68±0.02 | 9.42 | 73.9 |

**Fig. S5** compares the FDTD simulation (Lumerical FDTD) resutls with experiment. **Fig. S5**a shows refractive index profile of silicon and silicon metasurface in one period. Periodic boundary condition is applied in X direction and PML on Z direction. A plain wave source is applied with frequency span from 0.5-3 THz and propagates along Z axis. Mesh is auto non-uniform and minimum mesh step is 0.25 nm. An additional mesh is added to the doping layer with dx=50nm, dy=1um, and dz=50nm. Auto shutoff minimum is 5e-6 and simulation time is 100 ps. For the simplicity of simulation, we used the default pulse setting. A few approximations are taken in the simulation: the doped silicon layer has constant doping over 500 nm; the depletion region is replaced by intrinsic silicon; and the gap between doped silicon is 200 nm.

**Fig. S5**b shows normalized FDTD time domain traces of silicon and silicon metasurface in TE and TM configurations. The pulse profile in TM configuration is indeed modified. The frequency dependence of experimental and simulated transmission spectra has shown

qualitative similarity, seen in **Figs. S5**c,d. Given above simulation condition, the simulation results are good enough for qualitative comparison with experiment.

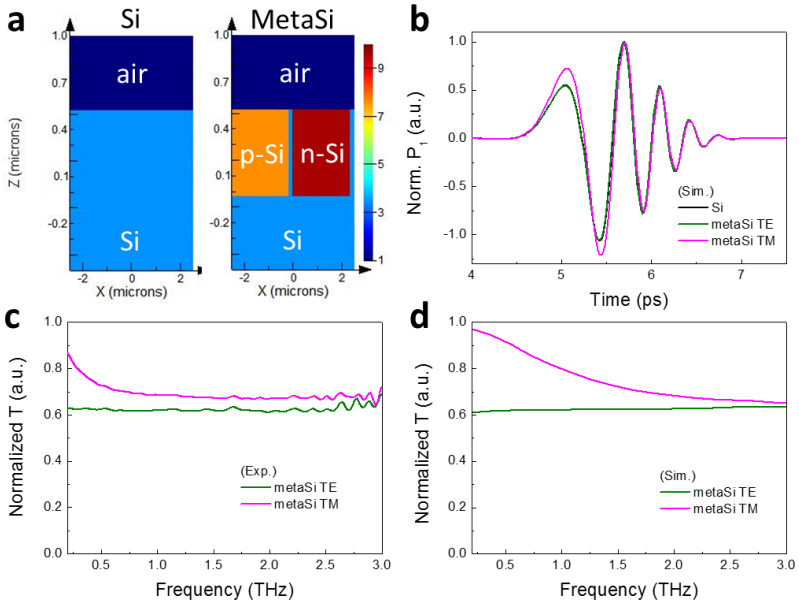


**Fig. S5**. a) FDTD refractive index profile of silicon and silicon metasurface in one period. b) Normalized FDTD time signal of silicon and silicon metasurface in TE and TM configurations. c,d) Experimental (c) and simulated (d) normalized transmission spectra calculated by FFT.

## S4. Temperature dependent THz-TDS spectroscopy

The THz-TDS system in **Fig. S6** is a commercial terahertz system (TPS Spectra 3000). THz beam is linearly polarized in vertical direction with the spectral range from 0.1 to 3 THz. The beam is focused on sample by a parabolic mirror with a divergence angle of 2.5/8. The sample is mounted on the cold finger of a Janis cryostat with the doped side in contact with the cold finger. The chamber is vacuumed using a mechanical pump (IDP-3) to avoid the absorption from atmospheric water vapor. Temperature range is from 300 to 350 K, which is controlled by Lakeshore 332 temperature controller. The acquired data are averaged from 900 spectra with a scanning frequency of 30 Hz, which gives a very high signal to noise ratio. Spectral resolution is 0.2 $cm^{-1}$.

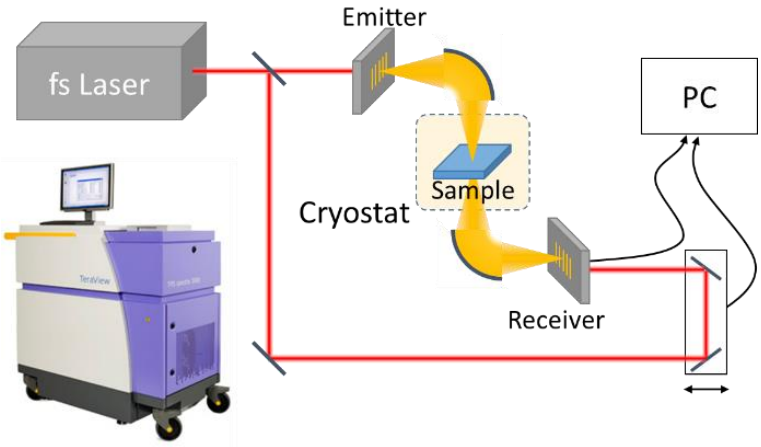


**Fig. S6**. Schematics of temperature dependent THz-TDS system using TPS Spectra 3000.

## S5. High temperature passive THz-TDS measurement

Temperature dependent THz-TDS measurement is carried out to understand the thermal influence on bias-voltage-dependent THz-TDS results. Time signals are compared between silicon, silicon with p-Si thin layer, and silicon metasurface in TE and TM configurations. Two distinct temperatures are selected 300 and 350 K. Higher temperature is not achievable due to the limitation of heating unit.

In silicon, heating results in a pure time delay of the terahertz pulses (**Fig. S7**). $P_1$ and $P_2$ shift laterally by +23 and +67 fs respectively for a temperature increment of $\Delta T$=50 K. The refractive index of silicon increases at a rate of $(1/n)(dn/dT) = 4.8\times10^{-5}$ $K^{-1}$ which agrees well with the published results.[8] It results in an insignificant change in reflection coefficient (~$10^{-3}$) at Si/air interface.

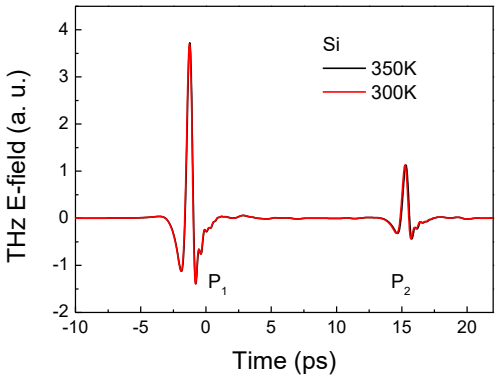


**Fig. S7**. Experiment time domain traces for silicon at 300 and 350 K.

In silicon with p-Si thin layer, heating not only results in time delay for $P_1$ but also increases its amplitude (**Fig. S8**a). Time delay is attributed to the slightly refractive index change in the silicon substrate. Increasing amplitude means decreasing real sheet conductivity of the doped layer, calculated as -0.28 mS for $\Delta T$=50 K. The reflection coefficient at Si/p-Si/air interface is totally changed by $22.2\times10^{-3}$ which is one order of magnitude higher than that of silicon. **Therefore, if one purposely dopes silicon thin layer to overcompensate the impedance mismatch between silicon and air, impedance matching can be achieved by increasing temperature and the total transmission will increase**. FDTD simulation is carried out on a similar structure. **Fig. S8**b is the refractive index profile of air/p-Si/Si at 300 and 400 K. **Fig. S8**c shows simulation results in time domain. The amplitude of pulse increases as expected.

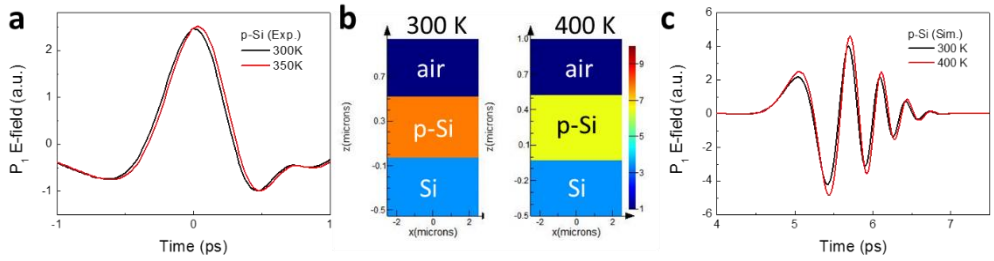


**Fig. S8**. a) Experiment time domain traces for p-Si at 300 and 350 K. b) Refractive index profile of air/p-Si/Si at 300 and 400 K. c) FDTD results for p-Si at 300 and 400 K.

**Fig. S9** plots the experimental and simulated temperature dependent THz-TDS results on silicon metasurface. In TE configuration, it has the same trend as that of p-Si. The calculated reflection coefficient of silicon metasurface is in total changed by $26.3 \times 10^{-3}$ which is comparable with that of p-Si. In TM configuration, amplitude of $P_1$ has non-uniform increment comparing to TE configuration. Simulation and experiment agree well with each other despite that THz pulse profiles are different.

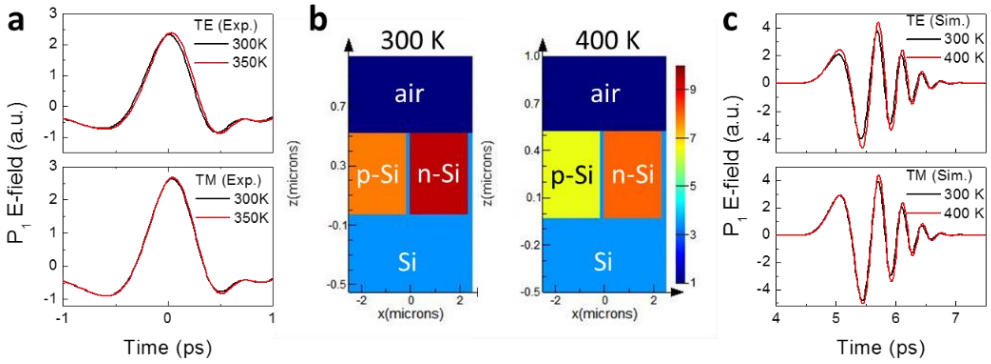


**Fig. S9**. a) Experiment time domain traces (TE/TM) for silicon metasurface at 300 and 350 K. b) Refractive index profile of air/metaSi/Si at 300 and 400 K. c) FDTD results for silicon metasurface at 300 and 400 K.

## S6. IVT measurement on active silicon metasurface

**Fig. S10**a plots an IV curve of the active silicon metasurface taken from -47.5 to 27.5 V. All data points are average values recorded within 20 s which is the integration time of individual THz-TDS measurement. The error bar indicates the variation of current at each fixed voltage. The current is nearly linear dependent on voltage with slightly different slope for forward and reverse bias. Due to the high doping concentration, the depletion region is very narrow and easily breaks down under reverse bias. Current is mainly limited by series resistance in n and p regions at large forward and reverse bias. Applying bias, the device is quickly heated by electric power (VI). **Fig. S10**b plots the surface temperature as a function of dissipated electric power ($I^2R$). Temperature linearly increases with dissipated power in forward and reverse bias at rate of dT/dP = 13.27 K/W and 15.16 K/W, respectively. It is typical Joule heating. The power conversion from applied electric power to the dissipated power is nearly 100% as shown in the inset of **Fig. S10**a.

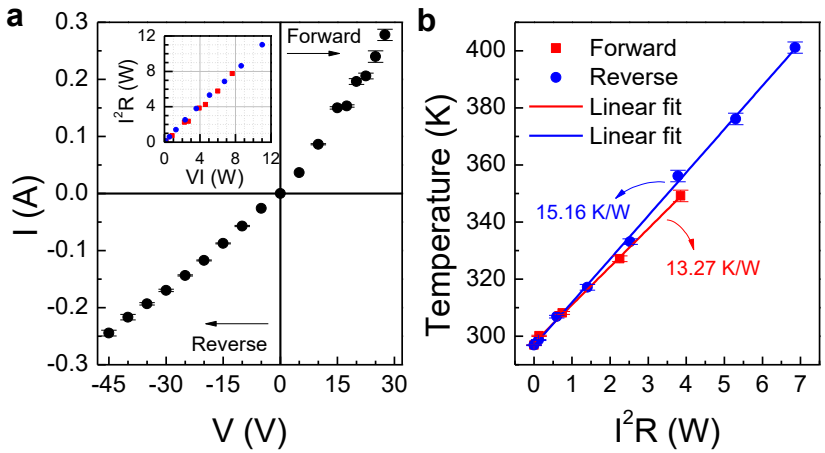


**Fig. S10**. a) IV result of the active silicon metasurface. Inset is plots the electric power conversion relation. b) Surface temperature as a function of dissipated electric power.

## S7. Temperature dependence of complex reflection coefficient of active silicon metasurface

The temperature dependence of complex reflection coefficient $r_C$ of silicon metasurface can be further understand analytically using effective medium model,[3] *e. g.* a three-layered system where metasurface structure is sandwiched between two dielectric media with different refractive indices. The schematics is shown in **Fig. S11**a. Only TE configuration is considered. Periodic and electromagnetic boundary conditions are applied to the electric and magnetic fields of the propagating terahertz wave in three individual layers along the OX and OZ directions, respectively. As a test of principle, the antireflection coating is only n-doped. Filling factor is f = 0.9. Taking doping concentration and mobility from **Table S1** and considering the fact that high temperature mobilities are limited by phonon scattering $\mu_{ph} \sim T^{-3/2}$, the calculated reflection coefficient is shown in **Fig. S11**b. $|r_C|$ has clear temperature dependence due to the temperature dependent conductivity. Interestingly, it cannot reach absolute zero. **Fig. S11**b inset shows the real $\mathrm{Re}(r_C)$ and imaginary $\mathrm{Im}(r_C)$ part of the reflection coefficient near the impedance matching point. It shows a finite $\mathrm{Im}(r_C)$ when $\mathrm{Re}(r_C)$ =0, which is due to the finite imaginary part of the complex conductivity.

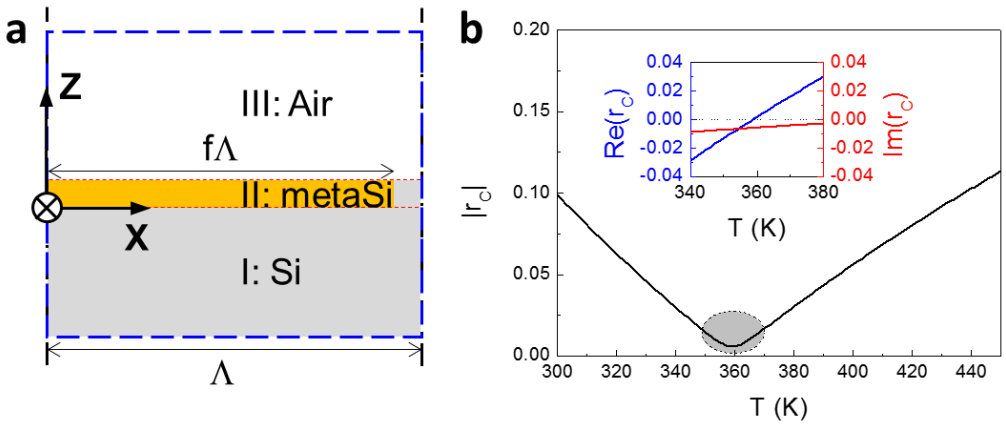


**Fig. S11**. a) Schematics of simulation geometry. b) Theoretically calculated $|r_C|$ as a function of temperature at 1 THz. Inset shows real $\mathrm{Re}(r_C)$ and imaginary $\mathrm{Im}(r_C)$ near the impedance matching point.

## S8. Transmission THz-TDS in TM configuration of active silicon metasurface

The device is mounted in TM configuration, where the longer side of silicon stripe is perpendicular to the polarization of the incident THz wave (**Fig. S12**a). $P_1$ and $P_2$ (**Figs. S12**b,c respectively) show the same waveform which is slightly modified comparing with that of silicon (**Fig. S3**a inset). Amplitude of $P_1$ and $P_2$ are bias-polarity dependent and the phase are delayed. The amplitude are calculated by FFT of the temporal waveform of the detected terahertz pulses which show strong interference fringes spectra (**Fig. S12**d). Therefore, in TM configuration, the silicon metasurface has tunability on terahertz amplitude and phase irrelevant to antireflection property.

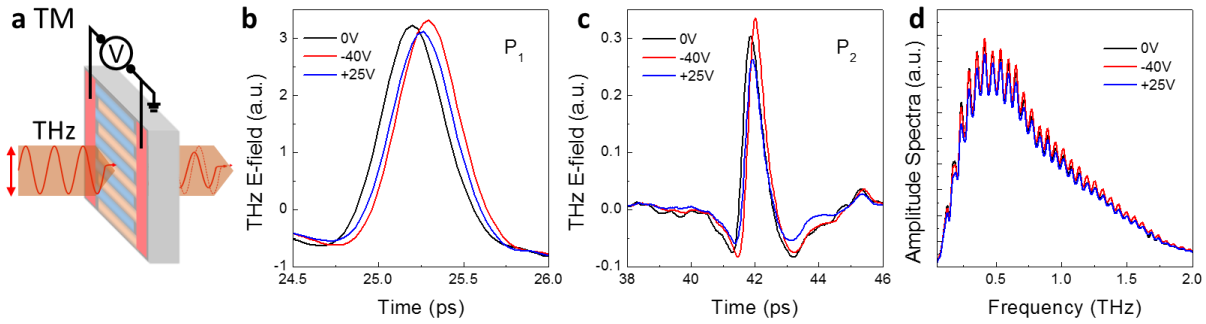


**Fig. S12.** a) Schematic of transmission THz-TDS in TM configuration. b-d) Time-domain traces of main pulse $P_1$ (b) and the first echo $P_2$ of the silicon substrate (c) at selected bias voltages, and amplitude spectra calculated by FFT (d).

## S9. Modulation speed of active silicon metasurface

The setup for electrical modulation experiment is shown in **Fig. S13**a. The DC power supply is set at 35 V. When applying bias voltage to the device, a Songle relay (maximum electrical switching frequency is 0.5 Hz) is wired between the DC power supply and the device in series configuration to switch bias between ON and OFF states. Switching frequency is controlled by a function generator which generates a TTL square wave between 0 and 5 V. The device is thus periodically reverse-biased between 0 and -35 V. Then, THz transmission pulse trains under modulated bias is monitored by an oscilloscope. Transmission peak intensity is extracted and normalized between 0 and 1, where 0 represents the static transmission level at 0V and 1 represents the static transmission level at -35 V.

**Fig. S13**b plots the variation of peak intensity at modulation frequency 0.1 Hz. The intensity increases/decreases when switching ON/OFF the reverse bias, respectively. After switching, the intensity takes about 2 s to stabilize. Since the modulation frequency is slower than the maximum switching frequency of the relay, the measured result is true device response.

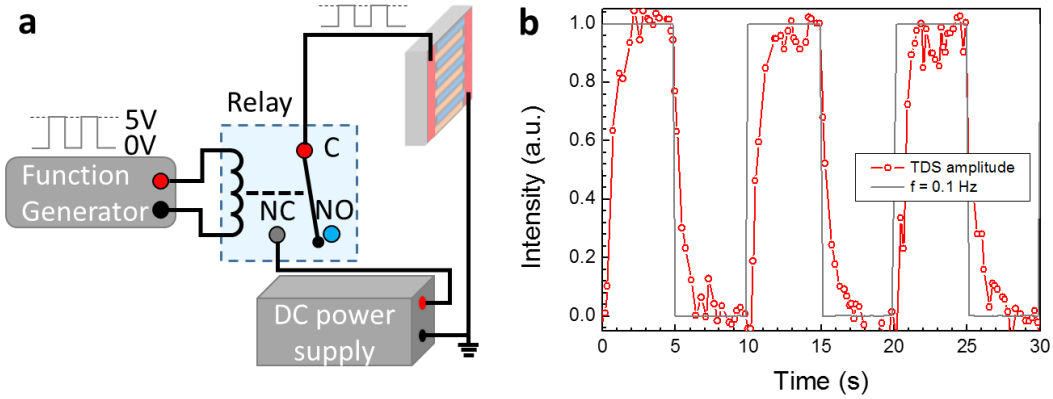


**Fig. S13**. a) Schematic of electrical modulation setup. A relay is wired in series configuration between DC power supply and the device to switch ON/OFF the voltage. C, NC, and NO are short for common, normally closed, and normally open. b) Normalized transmission modulated at 0.1 Hz.

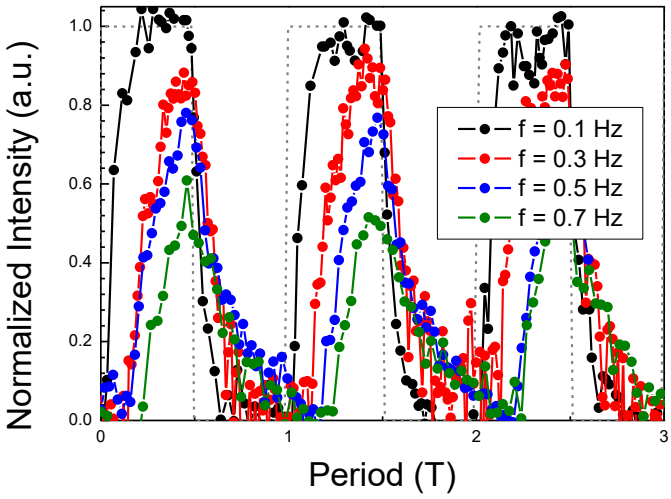


**Fig. S14**. Normalized transmission modulated at various frequency.

**Fig. S14** plots the normalized transmission modulated at 0.1 Hz, 0.3 Hz, 0.5 Hz, and 0.7 Hz. With increasing modulation frequency, the device shows obvious retardation at the rising and falling edges, and the amplitude cannot reach maximum before the circuit open. Slow modulation speed indicates that the nature of modulation is thermally based, which is due to the large size of the device and the inefficient heat dissipation via air. Therefore, the current device is only suitable for 'quasi-static' tuning.

## Supplementary References

[1] A. Thoman, A. Kern, H. Helm, M. Walther, *Phys. Rev. B* **2008**, 77, 195405.
[2] J. Dai, J. Zhang, W. Zhang, D. Grischkowsky, *J. Opt. Soc. Am. B* **2004**, 21, 1379.
[3] L. Ding, Q. Y. S. Wu, J. F. Song, K. Serita, M. Tonouchi, J. H. Teng, *Adv. Opt. Mater* **2013**, 1, 910.
[4] M. Tinkham, *Phys. Rev.* **1956**, 104, 845.
[5] a) T.-I. Jeon, D. Grischkowsky, *Phys. Rev. Lett.* **1997**, 78, 1106; b) S. Nashima, O. Morikawa, K. Takata, M. Hangyo, *Appl. Phys. Lett.* **2001**, 79, 3923.
[6] W. Spitzer, H. Fan, *Phys. Rev.* **1957**, 106, 882.
[7] G. Masetti, M. Severi, S. Solmi, *IEEE Trans. Electron Devices* **1983**, 30, 764.
[8] H. Li, *J. Phys. Chem. Ref. Data* **1980**, 9, 561.